JGR Oceans

RESEARCH ARTICLE
10.1029/2020JC016167

Azimuthal Dependence of GNSS-R Scattering Cross-Section in Hurricanes

Rajeswari Balasubramaniam[1] and **Christopher Ruf**[1]

[1]Climate and Space Science and Engineering Department, University of Michigan, Ann Arbor, MI, USA

Key Points:
- Azimuthal variations of GNSS-R scattering cross-section in hurricanes are modeled with sinusoidal harmonics
- The azimuthal harmonics explain 2–8% of the overall variation in scattering cross-section
- The magnitude of the azimuthal harmonics increases with increasing wind speed

Correspondence to:
R. Balasubramaniam,
rajibala@umich.edu

Citation:
Balasubramaniam, R., & Ruf, C. (2020). Azimuthal dependence of GNSS-R scattering cross-section in hurricanes. *Journal of Geophysical Research: Oceans*, *125*, e2020JC016167. https://doi.org/10.1029/2020JC016167

Received 19 FEB 2020
Accepted 12 JUN 2020
Accepted article online 18 JUN 2020

Abstract Global Navigation Satellite System-Reflectometry (GNSS-R) measurements of the ocean surface are sensitive to roughness scales ranging from a few cms to several kms. Inside a hurricane the surface roughness changes drastically due to varying sea age and fetch length conditions and complex wave-wave interactions caused by its cyclonic rotation and translational motion. As a result, the relationship between the surface roughness at different scale sizes becomes azimuthally dependent, as does the relationship between scattering cross-section and wind speed as represented by a Geophysical Model Function (GMF). In this work, the impact of this azimuthal variation on the scattering cross-section is assessed. An empirical GMF is constructed using measurements by the NASA CYclone GNSS (CYGNSS) matched to HWRF reanalysis surface winds for 19 hurricanes in 2017 and 2018. The analysis reveals a 2–8% variation in scattering cross-section due to azimuthal location, and the magnitude of the azimuthal dependence is found to grow with wind speed.

Plain Language Summary Global Navigation Satellite System-Reflectometry (GNSS-R) is a technique of studying reflected GPS signals to extract useful information about the surface. CYGNSS is the first of its kind GNSS-R constellation mission selected by NASAs earth venture program. The goal of the mission is to understand inner core processes in hurricanes by making accurate surface wind speed measurements there. Wind speed at the surface is determined using a GMF that maps the reflection measurement to a wind speed. Due to the complex nature of sea state and wave interactions inside a hurricane, measured scattering cross-section depends on the azimuthal location of the measurement inside the hurricane system. A modified GMF is proposed here that accounts for the azimuthal dependence. The model is developed by matching up CYGNSS measurements to hurricane winds estimated by the NOAA HWRF model for 19 hurricanes during 2017 and 2018. The new GMF accounts for a 2–8% variation in the measurements due to azimuthal location which increases with wind speed.

1. Introduction

The measurement of hurricane wind fields has a long history, ranging from airborne measurements (Jones et al., 1981; Uhlhorn et al., 2007; Wright et al., 2001) to spaceborne observations made by microwave radiometers and radars (Ebuchi et al., 2002; Figa-Saldaña et al., 2002; Gaiser et al., 2004). The key challenges for mapping the complex hurricane wind fields are the need for adequate spatial and temporal sampling of such fast evolving phenomena and the ability to penetrate through strong rain bands to measure the surface winds. Global Navigation Satellite System-Reflectometry (GNSS-R) is a relatively new field of remote sensing that uses the existing GNSS signals to study the surface. It greatly improves the sampling and revisit capability by utilizing the existing GPS transmitter constellation, and its L-band measurements are less affected by the heavy precipitation in the rain bands.

A GNSS-R system is a bistatic radar in a specular forward scattering geometry. A number of airborne (Garrison et al., 1998, 2002; Katzberg et al., 2001) and spaceborne GNSS-R systems (Foti et al., 2015; Gleason, 2013; Soisuvarn et al., 2016) have verified the ability of this configuration to successfully retrieve ocean surface winds from space. A GNSS-R radar measures the scattering cross-section of the surface around the region of specular reflection. The reflected GPS signal observed by a GNSS-R receiver is mapped into delay-doppler space for different time delays, and doppler shifts are observed. This forms the Delay-Doppler Map (DDM) of the surface (Gleason et al., 2009).

It is important to note that the scattering cross-section measured by a GNSS-R receiver is directly related to the surface roughness rather than the surface wind itself. GNSS-R forward scatter is quasi specular

incoherent scatter in most conditions. Thus an appropriate Mean Squared Slope (MSS) of the surface as sensed by GNSS-R measurements is an integration of the wave spectrum over a range of wavelengths ranging from several meters up to a few tens of cms. The surface MSS is inversely related to the measured normalized bistatic radar cross-section (σ_0). The Geophysical Model Function (GMF) maps this σ_0 to the ocean surface wind speed empirically to retrieve the near-surface wind speed from the measurements. In a hurricane environment, with complex temporal and spatial distribution of wind and wave fields, it is a challenging task to accurately retrieve wind speed from GNSS-R measurements. The scattering cross-section depends on surface roughness scales spanning a wide range from small capillary waves to long gravity waves. In fully developed seas, with essentially infinite sea age and fetch length, the relative magnitude of the surface roughness at different scale sizes reaches an equilibrium state due to energy cascade and dissipation mechanisms. Inside a hurricane, however, the sea age and fetch length conditions can vary significantly with azimuthal location due to its rotational and translational motion. This can perturb the balance between the roughness at different scales and alter the measured scattering cross-section. Despite its complex nature, several simulations (Fan et al., 2009; Moon et al., 2003; Young, 2017), directional buoy measurements (Young, 2006), and airborne missions (Uhlhorn et al., 2007; Walsh et al., 1985; Wright et al., 2001) have, over the years, helped develop directional wave spectra for hurricanes. The directional wave spectra acquired from several hurricane reconnaissance missions suggest that local wind and wave directions vary sinusoidally with the azimuth angle referenced to the hurricane heading and have a weak radial dependence (Hwang et al., 2017). These results suggest that remote sensing techniques such as GNSS-R, which depend on surface wave scattering, should consider azimuthal wind-wave response functions for accurate modeling and subsequent wind retrieval.

A GNSS-R GMF describes the relationship between measured scattering cross-section and the 10 m reference wind speed. Previous empirical GMFs for hurricane winds have been developed without allowing for possible dependence on azimuthal location within the storm (Clarizia et al., 2014; Ruf & Balasubramaniam, 2018). As a result, actual azimuthal dependencies are essentially averaged out, and wind speed retrieval errors will be correlated with azimuth location. An improved, azimuthally dependent, empirical GMF is developed here to better account for the azimuthal variation of the wind and wave directions. A large data set of observations from the CYGNSS mission is used. CYGNSS is a NASA mission that was launched in December 2016. It has eight microsatellites equally spaced around a 520 km circular orbit inclined at 35 degrees. Each satellite carries a GNSS-R radar receivers tuned to measure GPS L1 signals at 1.575 GHz, thereby enabling it to make measurements through heavy precipitation regions with a mean revisit time of 7 hr. The DDM measurements are made at a rate of 1 Hz and have continued uninterrupted since March 2017.

In this work, the impact of azimuthal variation on the measured scattering cross-section is assessed using CYGNSS data over 19 major hurricanes across different basins during 2017 and 2018. For this analysis, HWRF reanalysis hurricane winds are used as a reference. The remainder of this paper is structured as follows. Section 2 gives a description of the data sets used and the observations from the CYGNSS-HWRF matchup analysis. Section 3 describes the empirical GMF developed as a function of azimuth angle; Section 4 assesses the performance of the proposed model, and section 5 provides the conclusions of the study.

2. Theory and Observations

For this analysis, the v2.1 release of CYGNSS Level 1 σ_0 measurements over 19 major hurricanes from 2017 and 2018 is used (PO.DAAC, 2018). The data are matched to Hurricane Weather Research and Forecasting (HWRF) reanalysis winds of the inner nest grid spacing of 2 km. The HWRF winds are re-sampled to CYGNSS resolution and are empirically paired to CYGNSS σ_0 observations with a maximum temporal separation of 60 min and a maximum spatial separation of 0.25 deg lat and lon. The matchups are then translated into a storm-centric-direction of motion-based coordinate system for the purpose of understanding the azimuthal variation of measurements relative to the storm heading. The Weather Research and Forecast (WRF) system for hurricane prediction (HWRF) is an operational model developed by the National Centers for Environmental Prediction (NCEP). HWRF provides three domains (one parent and two nested) and is based on the initial position of the storm and on the National Hurricane Center (NHC) forecast of the

Table 1
Hurricanes From Different Basins in the CYGNSS-HWRF Matchup Data Set

West Pacific	East Pacific	Atlantic	Indian
Jebi	Aletta	Florence	Mekunu
Jelawat	Otis	Harvey	Titli
Mangkhut	Willa	Irma	
Maria		Jose	
Trami		Maria	
Walaka		Michael	
Yutu		Oscar	

72 hr storm position. The two nested domains move along the storm with a coverage of 24 deg × 24 deg and 7 deg × 7 deg for the middle nest and the inner nest, respectively (Tallapragada et al., 2014). For our purposes, we use the inner nest gridding that offers the finest resolution of about 0.015 deg (approximately 2 km). The CYGNSS level 1 σ_0 are also filtered by several quality measures for this analysis. Only observations with high antenna gain (>5 dB) and the overall quality flag set to best quality are used. This has allowed a total data set consisting of ~187,000 observations in hurricanes by CYGNSS. Table 1 lists the different hurricanes contained in this data set.

The CYGNSS wind retrieval algorithm uses the two measured observables, namely, the normalized bistatic radar scattering cross-section (σ_0) and the slope of the leading edge of the radar return pulse scattered by the ocean surface (LES) (Clarizia & Ruf, 2016). With these observables, GMFs are empirically derived by pairing near co-incident independent estimates of 10 m referenced ocean surface wind. For a fully developed sea (FDS), which constitutes the majority of the measurements, the observables are matched to the ground truth reference which is the combination of European Centre for Medium-Range Weather Forecasts (ECMWF) and Global Data Assimilation System (GDAS) reanalysis wind speed products. This results in a FDS GMF. For young sea conditions with limited fetch (YSLF), as observed in hurricanes, a YSLF GMF is generated using matchups with near co-incident NOAA P-3 hurricane hunter passes over the major Atlantic storms in 2017 (Ruf & Balasubramaniam, 2018).

Examples of the FDS and YSLF GMFs are shown in Figure 1 for observations at incidence angles of 10, 30, and 50 deg. Above wind speeds of ~15 m/s, the two GMFs diverge due to the underdeveloped state of seas near tropical cyclones, which tends to lower the roughness and increase the scattering cross-section. One important feature to note is the difference in the slope of the two GMFs at higher wind speeds. The YSLF GMF at high wind speeds has a higher value and a shallower slope (lower $|d\sigma_0/du10|$) for all incidence angles. In general, the high wind slope of the GMF can be used as a proxy for sea state development, with lower magnitudes being associated with younger seas.

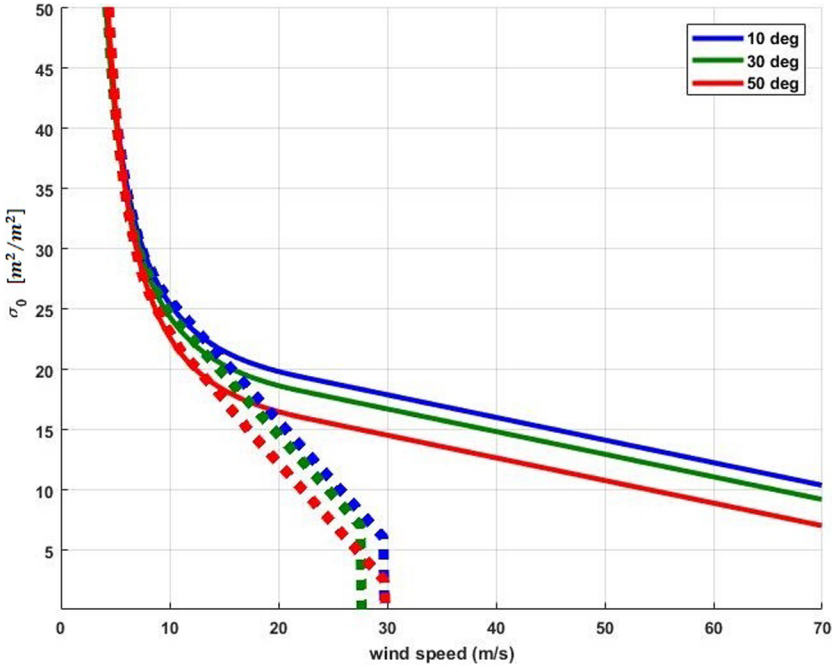

Figure 1. CYGNSS GMF for FDS winds shown by dotted lines and YSLF winds shown with solid lines. Incidence angles of 10, 30, and 50 deg are shown.

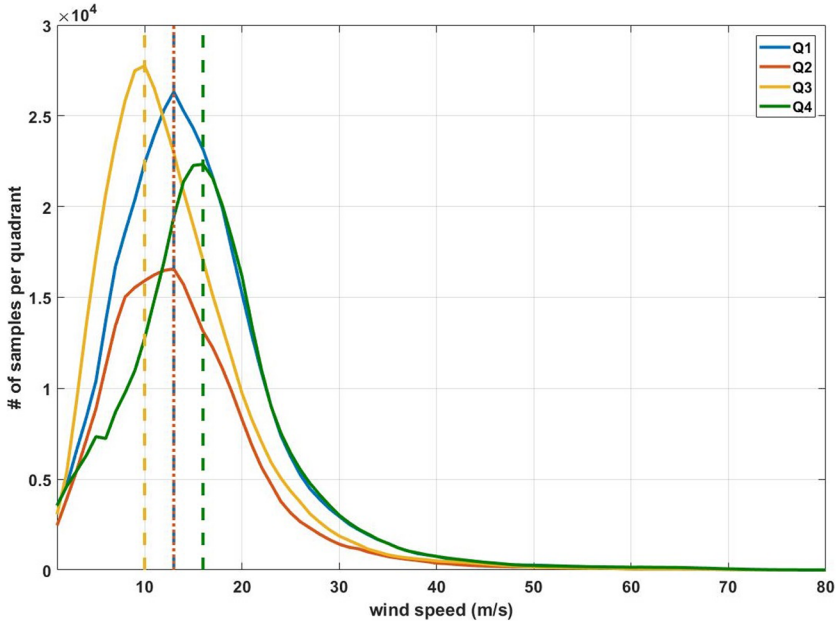

Figure 2. Distribution of winds in different quadrants in a storm relative to its heading.

Figure 2 shows the distribution of winds in different quadrants of a hurricane using the CYGNSS-HWRF matchup data set. The wind distribution inside the hurricane strongly varies in the azimuthal sense. In theory, the first quadrant is the generation region (shown in Figure 3a) and has the maximum energy. Also, Quadrant 1 has the largest wind speeds relative to the surface because the winds generated by the storm in this region are added to the storm motion. The wind generates a spectrum of waves with different group velocities. Waves that have their group velocity equal to the velocity of the forward motion of the storm remain in the intense wind region and receive maximum energy from the wind. Waves with group velocity greater than storm forward motion velocity will outrun the storm and propagate ahead as swell waves and those with a lower group velocity than the storm will be outrun by the storm and will be left behind

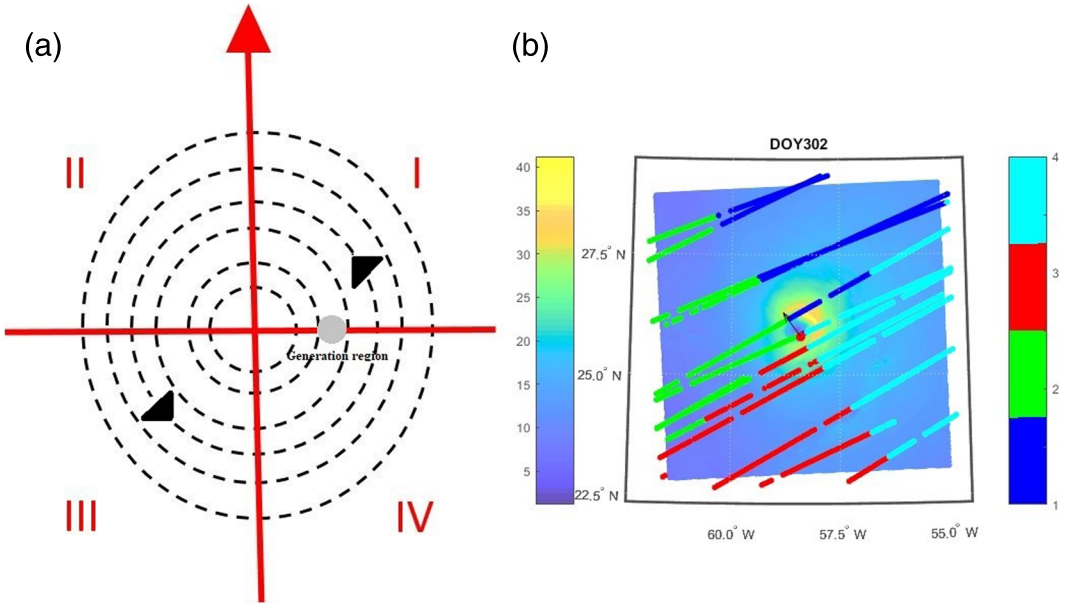

Figure 3. (a) Description of storm-centric-direction of motion-based coordinate system used in this paper. (b) Sample CYGNSS tracks overlaid on HWRF wind field. HWRF wind intensity is shown by the colorbar on the left, and the quadrant of the CYGNSS sample is shown by the colorbar on the right.

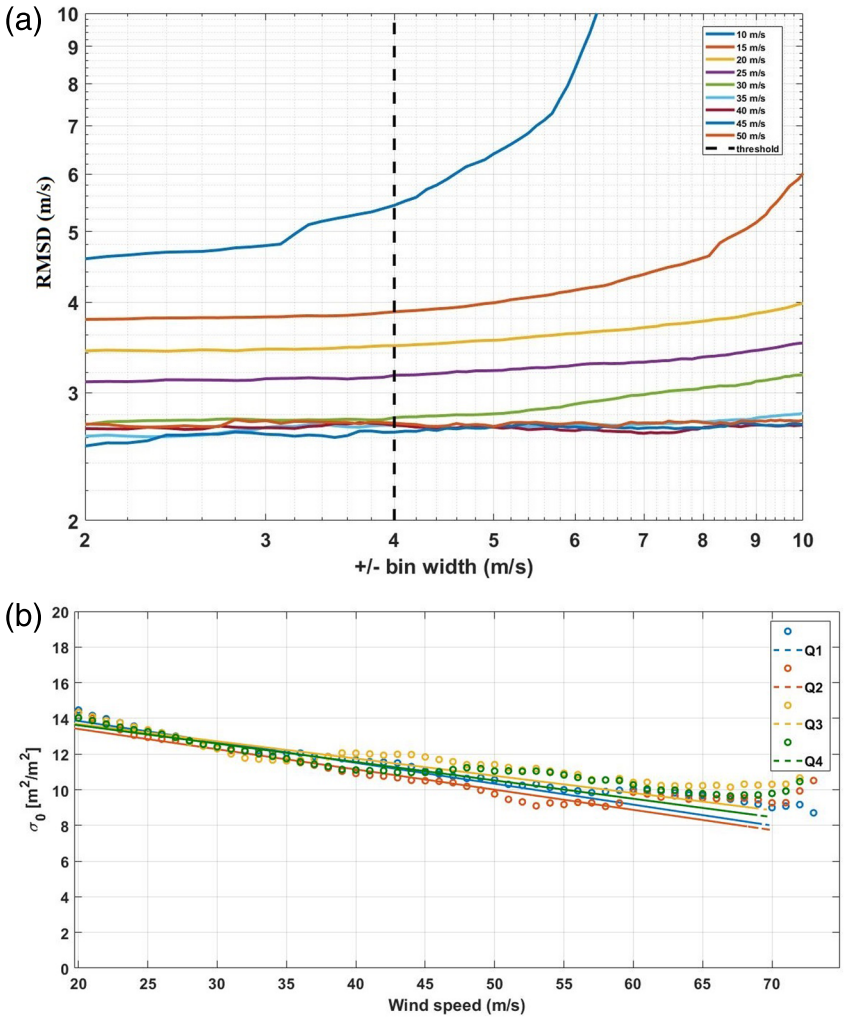

Figure 4. (a) Choice of wind speed averaging bin width based on RMS error. (b) GMF for different quadrants.

(Young, 1999). The swell radiating out ahead of the storm will often interact with the local calm sea in phase quadrature, resulting in a confused sea condition. This is generally observed ahead of the storm and to the rear of the storm, resulting in a younger sea in each of those regions.

The adequacy of a single slope for the GMF is assessed by determining the slope separately in each quadrant of a storm, relative to the storm heading. The storm quadrants are defined based on the Cartesian representation of quadrants with increasing azimuth angle in the anti-clockwise direction (see Figure 3a). An example track of CYGNSS overlaid on HWRF, partitioned by storm quadrant (color bar on the right) is shown in Figure 3b, the storm heading is represented by the black arrow at the storm center (identified by the red circle).

For the purpose of analysis, the range of HWRF wind speeds from 20 to 70 m/s is divided into bins. The center of each wind speed bin is stepped in 1 m/s increments from 20 to 70 m/s. Within a bin, all corresponding CYGNSS scattering cross-section measurements are averaged together. The wind speeds are binned in this way to reduce biases in the estimation process due to variations in sample size at different wind speeds. The width of each wind speed bin is chosen based on the RMS difference plot shown in Figure 4a. RMS difference is evaluated by

$$RMSD(w_i) = sqrt < (\sigma_{0i} - \overline{\sigma}0i)^2 > \quad (1)$$

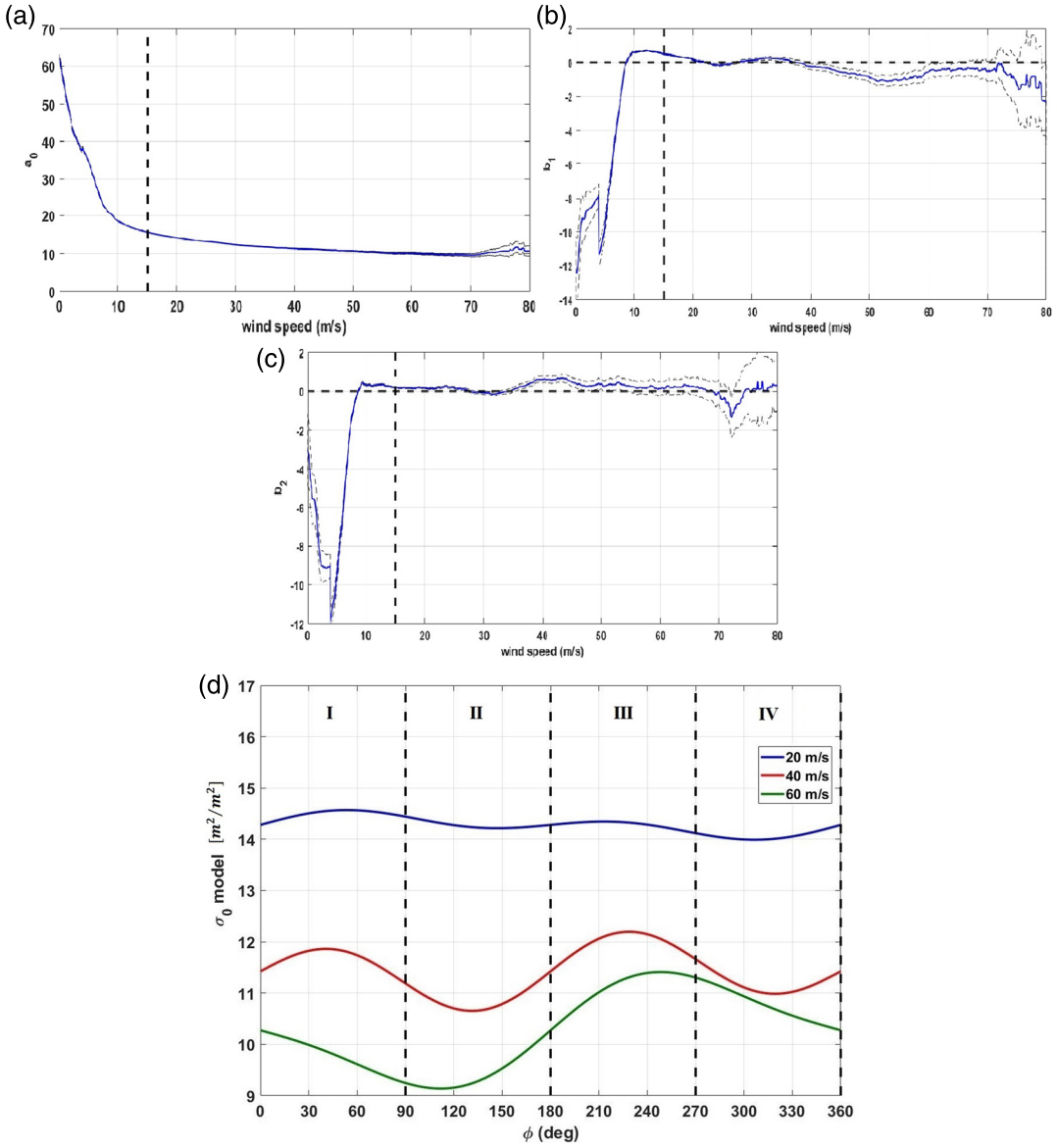

Figure 5. (a)–(c) Model parameters for azimuth GMF. (d) Azimuthal model for scattering cross-section shown for three different wind speeds.

Here $\boldsymbol{\sigma_{0i}}$ is the set of radar cross-section measurements in the ith wind bin, w_i and $\overline{\sigma}0i$ is the mean value of the cross-section in the given bin. The bin width is set as a variable parameter, and the error for different wind speed ranges and bin widths is plotted in Figure 4a. The RMS difference is found to be roughly constant for bin widths up to ±5 m/s; thus for optimal performance, we choose a width of ±4 m/s for the analysis throughout this paper. Figure 4b shows the GMF for different storm quadrants. The slope is derived by linear regression over the binned radar cross-section, as described above. These GMFs at high winds can be seen to vary with quadrants. This is consistent with the azimuthal variation of the local wind wave directions in published directional wavenumber spectrum data sets (B24, I09, I12, and I14) (Hwang et al., 2018). Quadrant 3 has the highest GMF, indicating a younger sea condition. Quadrant 2 has the lowest GMF, indicating an extended fetch and duration, therefore a longer sea age.

3. Harmonic Model Function

An empirical GMF is developed here which includes first- and second-order harmonic dependence on azimuthal location within the storm. This approach is based on the idea that any azimuthally varying

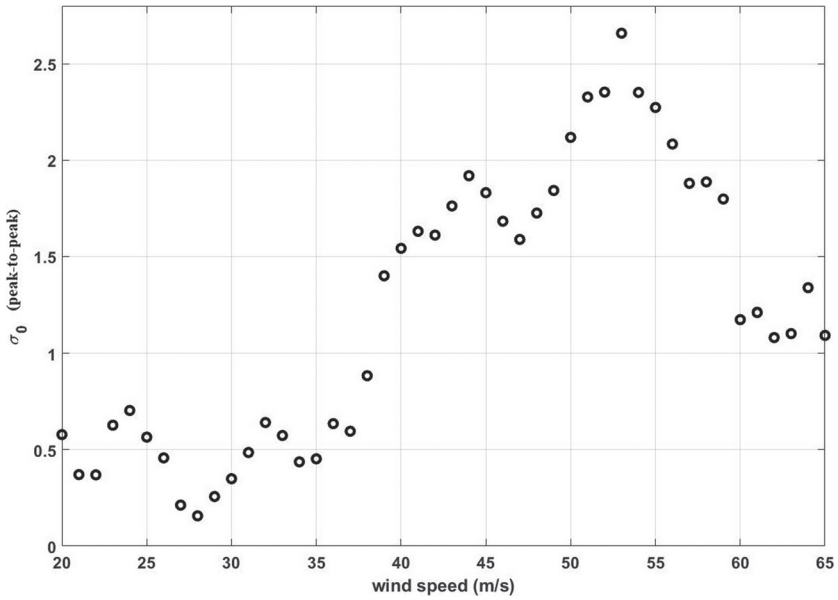

Figure 6. Peak-to-peak azimuthal variation of scattering cross-section for different wind speeds.

function can be modeled as a linear combination of sinusoids. This technique is commonly used to represent the azimuthal dependence of radar and radiometer observations of ocean surface winds (Meissner & Wentz, 2002; Wentz & Smith, 1999). The functional form of the model is given by

$$\sigma_0 = f(w, \varphi) = a_0(w) + b_1(w)sin(\varphi) + b2(w)sin(2\varphi) \quad (2)$$

where w is the wind speed, φ is the azimuth angle, and (a_0, b_1, b_2) are model parameters that depend on wind speed. Note that the slope of the GMF above ~20 m/s is the same for different incidence angles. Apart from the wind speed dependence of σ_0, it also has a dependence on incidence angle as shown in Figure 1. However, due to the limited size of the sample population, the dependence on incidence and azimuth angles cannot be separated. One way to address this issue is by maintaining a similar incidence angle distribution at all azimuth angles. This will mitigate the effect and the three-parameter harmonic model which results can be considered to represent the azimuthal dependence averaged across all incidence angles. It should be noted that the strength of the azimuthal dependence may vary with incidence angle. Additionally, note that if $b_1 = b_2 = 0$, the new GMF essentially defaults to the earlier azimuth-free version.

The σ_0 observations are averaged over wind speed bins which are $\pm$4 m/s wide, and the parametric model described above is fit to the observations for wind speed >15 m/s by nonlinear least squares minimization. The three model parameters (a_0, b_1, b_2) are shown versus wind speed in Figures 5a–5c. The estimated parameters are shown in blue, and the black-dashed lines represent the 95% confidence intervals on these estimates. Examples of the full GMF versus azimuth angle at 20, 40, and 60 m/s are shown in Figure 5d. Several important features of the GMF behavior can be observed. First, the magnitude of σ_0 decreases with increasing wind speed, similar to the previous GMF behavior. Secondly, the azimuthal dependence of the GMF increases with increasing wind speed. Thirdly, the maximum value of σ_0 occurs in the third quadrant for each wind speed, consistent with the GMF magnitude noted in Figure 4b. The minimum lies in the second quadrant, thus has a higher sea age and fetch conditions.

These effects are further illustrated in Figure 6, which plots the peak-to-peak azimuthal variation in σ_0 versus wind speed. The azimuthal variation rises steadily between ~30 and 55 m/s. The drop-off in azimuthal variation above 55 m/s may be a result of the small number of samples available and the lower sensitivity to changes in wind speed.

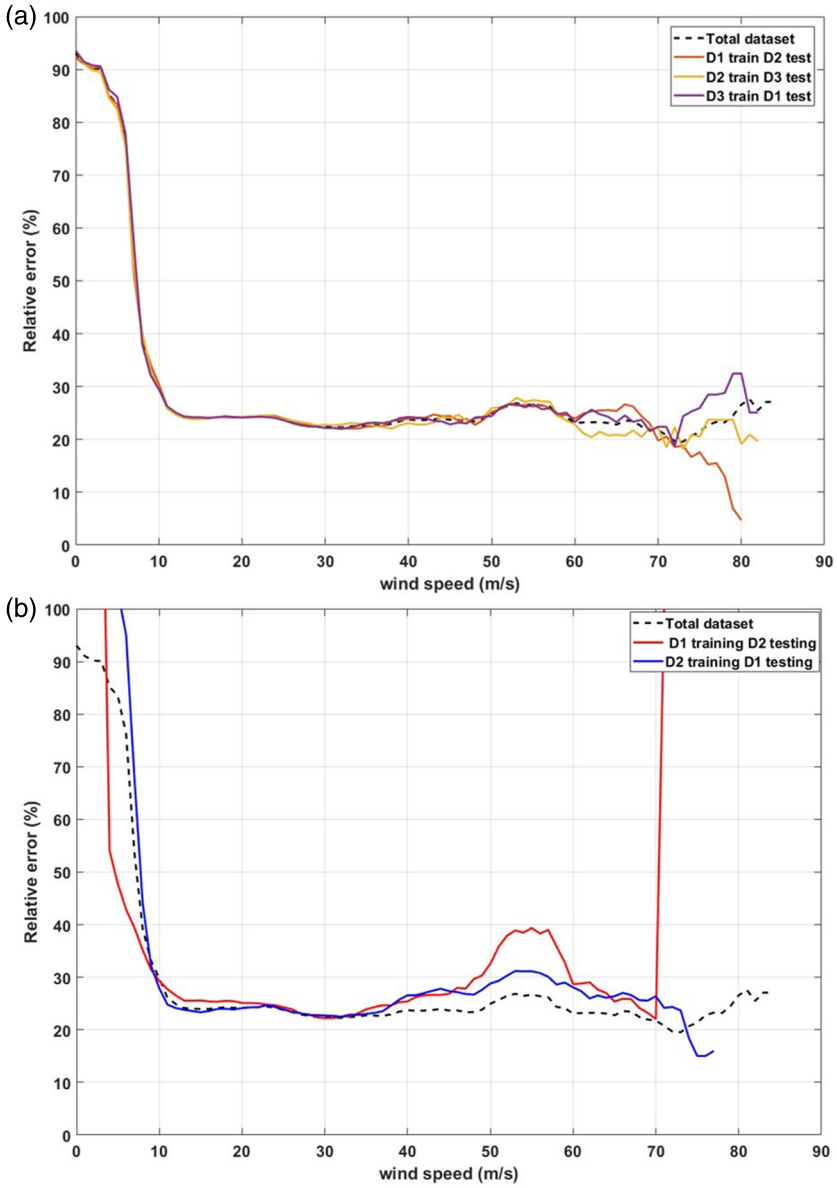

Figure 7. (a) RMSE for training and testing on three subsets (D1, D2, and D3). (b) RMSE for training and testing of two independent data sets (D1 and D2).

4. Performance Assessment

To assess the ability of the proposed model to capture the azimuthal variation in σ_0, several statistical measures of performance are considered. The robustness of the model is evaluated by breaking the total data set into three subsets using every third element. The model is then trained on one subset, and the relative RMSE is evaluated on another data set. This relative error formulation is given by

$$RealtiveError(\%) = \frac{\sqrt{<(\sigma_0 - \widetilde{\sigma}_0)^2>}}{<\sigma_0>} * 100 \tag{3}$$

Here σ_0 is the measurement sample at a given wind speed bin and $\widetilde{\sigma}_0$ is the model estimate of scattering cross-section for a given wind speed and azimuth information. Figure 7a shows the behavior of relative error versus wind speed for the different combinations of training and testing subsets. The dashed line represents

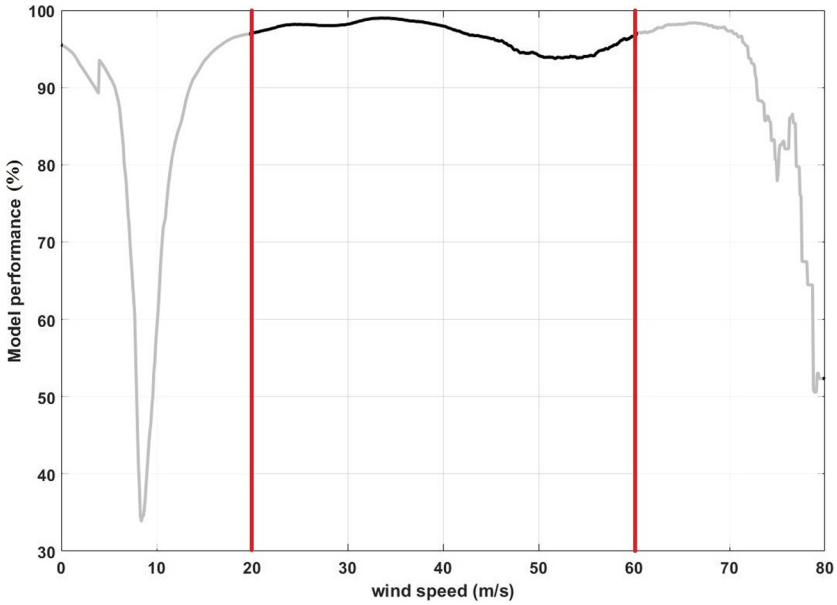

Figure 8. Evaluation of azimuthal information captured by the model.

the use of the total data set and hence is a test of internal consistency in the generation of the GMF. The large relative error at the lower wind speeds (<15 m/s) is due to the fact that the model has been trained only for higher wind speeds.

The relative error is consistent over the three different data sets (D1, D2, and D3) as well as over the total data set thus indicating the robustness of the developed model. Also, for wind speeds >60 m/s the relative error becomes noisy, and this is attributed to the sparse observations at such high winds. Next, the data set is divided into two independent subsets (D1 and D2) with storms well mixed from different basins and years, and the analysis is repeated. The result is shown in Figure 7b. The relative error is consistent over a wide range of wind speeds from 20 to 60 m/s re-attesting to the robustness of the model.

The next performance metric is a statistical measure of the percentage of azimuthal variation captured by the model over different wind speed ranges. The metric used for this purpose is given by

$$1-\frac{\mathbf{var}(\widetilde{\sigma}_0)}{\mathbf{var}(\sigma_0)}*100=\begin{cases}1, & \text{if model captures azimuth information completely.}\\ 0, & \text{if model does not capture any azimuth information.}\end{cases} \tag{4}$$

Here **var(.)** refers to the variance of the sample population, σ_0 is the measurements and $\widetilde{\sigma}_0$ the model. The assumption behind this statistical metric is that the total variance in the observations at a given wind speed is associated with multiple factors, one of which is azimuthal variation. Since the model explicitly accounts for azimuthal variation, any residual variance in the model should be due to other factors than azimuthal variation. If the metric is 1, it indicates that the model has captured all of the azimuth information, and if the metric is 0, no azimuth information is captured. Figure 8 shows the behavior of this metric tested for different wind speeds. The metric suggests that the model is consistent and is able to capture greater than 90% of the azimuthal variation over a broad range of wind speeds between 20 and 60 m/s. Lower wind speeds are shown here for completeness, and again, at higher winds the performance drops due to sparse observations in the region.

Finally, we evaluate the total error in the observed scattering cross-section due to the azimuthal variation. The measure is defined by

$$Error(\%)=abs\left(1-\frac{\mathbf{MSD}(\sigma_0,\widetilde{\sigma}_0)}{\mathbf{var}(\sigma_0)}\right)*100 \tag{5}$$

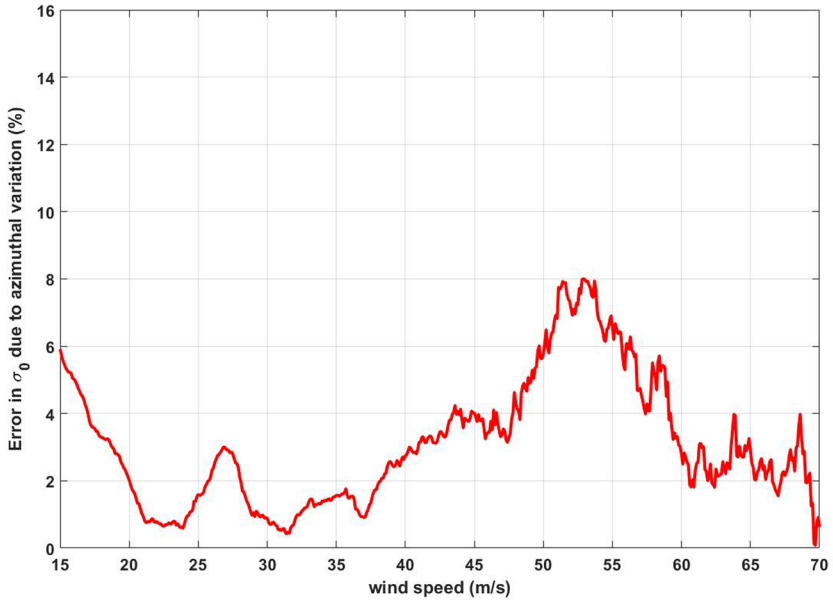

Figure 9. Error associated with scattering cross-section due to azimuthal variation.

Here, **MSD(.)** is the mean squared difference between the observations and the model estimate for a given wind speed, and **var(.)** is the total variance in the observation for a given wind speed. If the MSE between the observation and the model is the same as the variance in the observation, it suggests that no azimuthal error is observed, and if the MSE is negligible compared to the total variance in the observation, then most of the error in the σ_0 can be associated to azimuthal variation. Figure 9 shows the % error in the scattering cross-section caused by the azimuthal variation. The model suggests a 2–8% error in the scattering cross-section for the wind speed range 20–60 m/s. The error is close to 2% at 20 m/s and gradually increases to 8% around 53 m/s, then begins to reduce above that. While the overall error due to azimuthal variation is negligible, understanding the effect of this variation gives important insight into the wave properties inside a hurricane and its impending impact on the scattering cross-section. The increase in azimuthal variation with increase in wind speed also suggests that the GNSS-R scattering cross-section could be sensitive to the directional properties of wind at higher wind speed ranges.

5. Discussion and Conclusion

The specular bistatic scattering cross-section of the ocean surface in tropical cyclones, as measured by GNSS-R radar receivers on the CYGNSS spacecraft, is found to depend on azimuthal location relative to the direction of storm motion. The dependence is caused by variations in the sea age and fetch length with storm quadrant, which affects the balance between surface roughness at short (capillary) and long (gravity) wavelengths. The roughness spectrum, in turn, affects the scattering cross-section. A modified GMF is developed using a second-order harmonic expansion to represent the azimuthal dependence. The zeroth-order term in the GMF is consistent with previous models which have not included an azimuthal dependence. The first- and second-order terms together explain between 2% and 8% of the total variance in the scattering cross-section, with higher explained variance being associated with higher wind speeds. The azimuthal corrections to the GMF are found to be significant above ~20 m/s. Above ~60 m/s, the results are inconclusive owing to the scarcity of samples.

It is worthwhile to note that the current GMF used by the CYGNSS project does not include an azimuthal dependence in organized storms. Another difference from the GMF developed here is the source of reference winds. The v2.1 GMF was developed using matchups with near-surface wind measurements made by the Stepped Frequency Microwave Radiometer on NOAA hurricane hunter aircraft (Ruf & Balasubramaniam, 2018), whereas the GMF developed here uses matchups with HWRF model winds. Differences in overall magnitude between the two GMFs are likely a result of these differences.

The azimuthally dependent GMF has utility in two regards. It can serve as an indicator of sea state development in the inner core of tropical cyclones, for use in process studies into air-sea and wind-wave interactions. It could also be used to improve wind speed retrieval algorithms in tropical cyclones that are based on GNSS-R observations. Retrieval algorithms essentially invert the GMF to estimate wind speed given the scattering cross-section, and a more physically representative forward GMF will allow for a more accurate inversion. This type of study can also be extended to other non-TC weather systems with younger seas or scenarios with limited fetch conditions, for example, limited fetch on the lee side of major islands that may result in a different relationship between wind speed and MSS or σ_0 and therefore require a modified GMF for accurate wind speed retrieval. The next steps in this work will be to implement the proposed azimuthal GMF for CYGNSS wind retrieval and evaluate its performance.

Data Availability Statement

The Cyclone Global Navigation Satellite System (CYGNSS) Level 1 Science data record version 2.1 were obtained from the NASA EOSDIS Physical Oceanography Distributed Active Archive Center (PO.DAAC) at the Jet Propulsion Laboratory, Pasadena, CA (doi: 10.5067/CYGNS-L1X21). The HWRF reanalysis model data were obtained from the NOAA/NWS/NCEP/ Environmental Modeling Center (https://www.nco.ncep.noaa.gov/pmb/products/hur).

Acknowledgments
The work presented was supported in part by NASA Science Mission Directorate contract NNL13AQ00C with the University of Michigan.

References

Clarizia, M. P., & Ruf, C. S. (2016). Wind speed retrieval algorithm for the cyclone global navigation satellite system (CYGNSS) mission. *IEEE Transactions on Geoscience and Remote Sensing*, *54*(8), 4419–4432.

Clarizia, M. P., Ruf, C. S., Jales, P., & Gommenginger, C. (2014). Spaceborne GNSS-R minimum variance wind speed estimator. *IEEE Transactions on Geoscience and Remote Sensing*, *52*(11), 6829–6843.

Ebuchi, N., Graber, H. C., & Caruso, M. J. (2002). Evaluation of wind vectors observed by QuikSCAT/SeaWinds using ocean buoy data. *Journal of Atmospheric and Oceanic Technology*, *19*(12), 2049–2062.

Fan, Y., Ginis, I., Hara, T., Wright, C. W., & Walsh, E. J. (2009). Numerical simulations and observations of surface wave fields under an extreme tropical cyclone. *Journal of Physical Oceanography*, *39*(9), 2097–2116.

Figa-Saldaña, J., Wilson, J. J. W., Attema, E., Gelsthorpe, R., Drinkwater, M. R., & Stoffelen, A. (2002). The advanced scatterometer (ASCAT) on the meteorological operational (MetOp) platform: A follow on for european wind scatterometers. *Canadian Journal of Remote Sensing*, *28*(3), 404–412.

Foti, G., Gommenginger, C., Jales, P., Unwin, M., Shaw, A., Robertson, C., & Rosello, J. (2015). Spaceborne GNSS reflectometry for ocean winds: First results from the UK TechDemoSat-1 mission. *Geophysical Research Letters*, *42*, 5435–5441. https://doi.org/10.1002/2015GL064204

Gaiser, P. W., St Germain, K. M., Twarog, E. M., Poe, G. A., Purdy, W., Richardson, D., et al. (2004). The WindSat spaceborne polarimetric microwave radiometer: Sensor description and early orbit performance. *IEEE Transactions on Geoscience and Remote Sensing*, *42*(11), 2347–2361.

Garrison, J. L., Katzberg, S. J., & Hill, M. I. (1998). Effect of sea roughness on bistatically scattered range coded signals from the Global Positioning System. *Geophysical Research Letters*, *25*(13), 2257–2260.

Garrison, J. L., Komjathy, A., Zavorotny, V. U., & Katzberg, S. J. (2002). Wind speed measurement using forward scattered GPS signals. *IEEE Transactions on Geoscience and Remote Sensing*, *40*(1), 50–65.

Gleason, S. (2013). Space-based GNSS scatterometry: Ocean wind sensing using an empirically calibrated model. *IEEE Transactions on Geoscience and Remote Sensing*, *51*(9), 4853–4863.

Gleason, S., Gebre-Egziabher, D., & Egziabher, D. G. (2009). GNSS applications and methods.

Hwang, P. A., Fan, Y., Ocampo-Torres, F. J., & García-Nava, H. (2017). Ocean surface wave spectra inside tropical cyclones. *Journal of Physical Oceanography*, *47*(10), 2393–2417.

Hwang, P. A., Fan, Y., & Walsh, E. J. (2018). Hurricane hunter observations of wind and wave spectral properties: Implications on tropical cyclone remote sensing. In *Igarss 2018-2018 IEEE International Geoscience and Remote Sensing Symposium* (pp. 149–152). Valencia, Spain.

Jones, W. L., Black, P. G., Delnore, V. E., & Swift, C. T. (1981). Airborne microwave remote-sensing measurements of Hurricane Allen. *Science*, *214*(4518), 274–280.

Katzberg, S. J., Walker, R. A., Roles, J. H., Lynch, T., & Black, P. G. (2001). First GPS signals reflected from the interior of a tropical storm: Preliminary results from hurricane Michael. *Geophysical Research Letters*, *28*(10), 1981–1984.

Meissner, T., & Wentz, F. (2002). An updated analysis of the ocean surface wind direction signal in passive microwave brightness temperatures. *IEEE Transactions on Geoscience and Remote Sensing*, *40*(6), 1230–1240.

Moon, I.-J., Ginis, I., Hara, T., Tolman, H. L., Wright, C. W., & Walsh, E. J. (2003). Numerical simulation of sea surface directional wave spectra under hurricane wind forcing. *Journal of Physical Oceanography*, *33*(8), 1680–1706.

PO.DAAC, C. Y. G. N. S. S. (2018). *CYGNSS level 1 science data record version 2.1. ver. 2.1*. CA, USA: PO.DAAC. https://doi.org/10.5067/CYGNS-L1X21

Ruf, C. S., & Balasubramaniam, R. (2018). Development of the CYGNSS geophysical model function for wind speed. *IEEE Journal of Selected Topics in Applied Earth Observations and Remote Sensing*, *12*(1), 66–77.

Soisuvarn, S., Jelenak, Z., Said, F., Chang, P. S., & Egido, A. (2016). The GNSS reflectometry response to the ocean surface winds and waves. *IEEE Journal of Selected Topics in Applied Earth Observations and Remote Sensing*, *9*(10), 4678–4699.

Tallapragada, V., Bernardet, L., Biswas, M. K., Ginis, I., Kwon, Y., Liu, Q., et al. (2014). Hurricane weather research and forecasting (HWRF) model: 2013 scientific documentation (*99*): HWRF Development Testbed Center Tech. Rep.

Uhlhorn, E. W., Black, P. G., Franklin, J. L., Goodberlet, M., Carswell, J., & Goldstein, A. S. (2007). Hurricane surface wind measurements from an operational stepped frequency microwave radiometer. *Monthly Weather Review*, *135*(9), 3070–3085.

Walsh, E. J., Hancock III, D. W., Hines, D. E., Swift, R. N., & Scott, J. F. (1985). Directional wave spectra measured with the surface contour radar. *Journal of Physical Oceanography*, *15*(5), 566–592.

Wentz, F. J., & Smith, D. K. (1999). A model function for the ocean-normalized radar cross section at 14 GHz derived from NSCAT observations. *Journal of Geophysical Research*, *104*(C5), 11,499–11,514.

Wright, C. W., Walsh, E. J., Vandemark, D., Krabill, W. B., Garcia, A. W., Houston, S. H., et al. (2001). Hurricane directional wave spectrum spatial variation in the open ocean. *Journal of Physical Oceanography*, *31*(8), 2472–2488.

Young, I. R. (1999). *Wind Generated Ocean Waves*. Amsterdam: Elsevier.

Young, I. R. (2006). Directional spectra of hurricane wind waves. *Journal of Geophysical Research*, *111*, C08020. https://doi.org/10.1029/2006JC003540

Young, I. R. (2017). A review of parametric descriptions of tropical cyclone wind-wave generation. *Atmosphere*, *8*(10), 194.